

FAR-UV HST SPECTROSCOPY OF AN UNUSUAL HYDROGEN POOR SUPERLUMINOUS SUPERNOVA: SN2017EGM

LIN YAN¹, D. A. PERLEY², A. DE CIA³, R. QUIMBY⁴, R. LUNNAN⁵, KATE H. R. RUBIN⁴, P. J. BROWN⁶

¹Caltech Optical Observatories and IPAC, California Institute of Technology, Pasadena, CA 91125, USA; email: lyan@caltech.edu

²Astrophysics Research Institute, Liverpool John Moores University, IC2, Liverpool Science Park, 146 Brownlow Hill, Liverpool L3 5RF, UK

³European Southern Observatory, Karl-Schwarzschild Str. 2, 85748 Garching bei Muenchen, Germany

⁴Department of Astronomy, San Diego State University, San Diego, CA 92182, USA

⁵Oskar Klein Center, Astronomy Department, Stockholm University, SE-106 91 Stockholm, Sweden and

⁶George P. and Cynthia Woods Mitchell Institute for Fundamental Physics & Astronomy, Texas A. & M. University, Department of Physics and Astronomy, 4242 TAMU, College Station, TX 77843, USA

Draft version April 18, 2018

ABSTRACT

SN2017egm is the closest ($z = 0.03$) H-poor superluminous supernova (SLSN-I) detected to date, and a rare example of an SLSN-I in a massive, metal-rich galaxy. We present the *HST* UV & optical spectra covering $1000 - 5500 \text{ \AA}$ taken at +3 day relative to the peak. Our data reveal two absorption systems at redshifts matching the host galaxy NGC3191 ($z = 0.0307$) and its companion galaxy ($z = 0.0299$) $73''$ apart. Weakly damped Lyman- α absorption lines are detected at these two redshifts, with HI column densities of $(3.0 \pm 0.8) \times 10^{19}$ and $(3.7 \pm 0.9) \times 10^{19} \text{ cm}^{-2}$ respectively. This is an order of magnitude smaller than HI column densities in the disks of nearby galaxies ($> 10^{10} M_{\odot}$) and suggests that SN2017egm is on the near side of NGC 3191 and has a low host extinction ($E(B - V) \sim 0.007$). Using unsaturated metal absorption lines, we find that the host of SN2017egm probably has a solar or higher metallicity and is unlikely to be a dwarf companion to NGC 3191. Comparison of early-time UV spectra of SN2017egm, Gaia16apd, iPTF13ajg and PTF12dam finds that the continuum at $\lambda > 2800 \text{ \AA}$ is well fit by a blackbody, whereas the continuum at $\lambda < 2800 \text{ \AA}$ is considerably below the model. The degree of UV suppression varies from source to source, with the 1400 \AA to 2800 \AA continuum flux ratio of 1.5 for Gaia16apd and 0.4 for iPTF13ajg. This can not be explained by the differences in magnetar power or blackbody temperature. Finally, the UV spectra reveal a common set of seven broad absorption features and their equivalent widths are similar (within a factor of 2) among the four events.

Subject headings: stars: supernovae: individual: SN2017egm, Gaia16apd, PTF12dam, iPTF13ajg

1. INTRODUCTION

The spectra of hydrogen-poor superluminous supernovae (SLSNe-I) peak, and show their most distinctive spectroscopic features, in the ultraviolet (Quimby et al. 2011). These wavelengths are inaccessible from the ground, except at high redshift where the vast distances limit the S/N that can be achieved. Space-based UV spectra can cover these features for nearby SNe, but the limited sensitivity of UV spectrographs (even *HST*) restricts observations to very nearby and rare events. Up until now only one high-quality far-UV spectrum of a SLSN has been taken (Gaia16apd at $z = 0.102$; Yan et al. 2017).

Knowledge of the FUV spectra of SLSNe is important for several reasons: not only to investigate the structure and composition of the photosphere, but also to improve modeling of SLSN light curves and measure the bolometric energy release. Physical parameters are usually derived by fitting bolometric light curves (LC), estimated from broadband optical photometry in two or three filters. One of the significant uncertainties in this process is bolometric correction, especially at early times when as much as 50% of the bolometric luminosity is likely to escape in the UV. Many previously published studies have relied on either crude pseudo-bolometric LCs (summing up the available optical bands), or by assum-

ing a blackbody spectral energy distribution (SED), even though these events are known to have broad, deep UV absorption features (Quimby et al. 2011).

More recently, Nicholl et al. 2017c; De Cia et al. 2017b compute magnetar model parameters for a large sample of SLSNe-I by applying a single SED template to broad band light curves. This SED template is derived for the purpose of fitting broad band photometry. It does not match well with the *spectral continuum* of Gaia16apd. Broad band SEDs are affected by both continuum and broad, prominent absorption features (Yan et al. 2017). The focus of this paper is new in its investigation of how UV spectra vary among different SLSN-I, including both spectral continuum and absorption features.

SN2017egm (Gaia17biu) exploded in NGC 3191 at a distance of 140 Mpc ($z = 0.030$), making it the closest known SLSN-I by a large margin (Delgado et al. 2017; Dong et al. 2017). This offers an excellent opportunity to study the UV spectrum of an SLSN-I in detail, and to examine the diversity of this class at these wavelengths.

A particularly notable aspect of SN2017egm beyond its sheer proximity is its unusual location: the host is a large spiral galaxy with stellar mass $M_* \sim 10^{10.7} M_{\odot}$ and metallicity $Z \sim (1.3 - 2) Z_{\odot}$ (Nicholl et al. 2017a; Bose et al. 2017). This seems to argue against the consensus from several previous studies that almost all SLSNe-I occur in dwarf host galaxies with low metal abundances

($M_{star} \leq 10^{9.7} M_{\odot}$ and $Z \leq \sim 0.4 Z_{\odot}$) (Lunnan et al. 2014; Leloudas et al. 2015; Perley et al. 2016; Schulze et al. 2016; Chen et al. 2017a). SLSNe-I have been observed in high-mass hosts before, but only far from the center, and it has been argued that the metallicity at the SLSN site could still be low in these cases (Perley et al. 2016). The projected position of SN2017egm is very close to the host nucleus, and archival integral field unit (IFU) spectra of NGC 3191 make it possible to zoom in onto the spiral arm region where the supernova exploded, and measure the nebular gas-phase metallicities with a resolution of ~ 1 kpc. Two independent groups have found conflicting results, one with solar to super-solar metallicity (Chen et al. 2017b), and the other sub-solar metallicity (Izzo et al. 2017).

In this paper we present our HST far- and near-UV spectra of SN2017egm, and compare this event with the only pre-existing FUV SLSN spectrum (Gaia16apd) as well as two other high-quality near-UV SLSN spectra. We also exploit the narrow absorption transitions seen in our spectra to constrain the kinematics and chemical abundances of the system, providing confirmation (independent of emission-based methods) that the SN occurred along a metal-rich sightline and suggesting that SLSN production is not fully suppressed at high-metallicity.

2. HST DATA

SN2017egm was first discovered as a transient on 2017 May 23 UT by the Gaia Photometric Survey (Gaia Collaboration et al. 2016; Delgado et al. 2017). Optical spectra taken on May 30, 2017 UT by Dong et al. (2017) classified this event as a SLSN-I. We immediately triggered our approved *HST* ToO program (PID: 14674, Quimby), using both the Cosmic Origin Spectrograph (COS) and the Space Telescope Imaging Spectrograph (STIS) on board *HST*. Our single-epoch UV spectrum was obtained 2017 June 23 (MJD = 57927 d); the estimated peak and explosion dates are MJD = 57924 and 57890 respectively (Nicholl et al. 2017a), leading to the time lag between the *HST* UV spectra and the explosion date, Δt_{exp} of 35.9 day (rest-frame). As listed in Table 1, the COS and STIS spectra were taken with G140L, G230L and G430L gratings with moderate spectral resolutions. At 1500Å the *HST* COS spectra have a velocity FWHM of ~ 120 km s $^{-1}$. We use the reduced spectra provided by the *HST* pipelines.

Our analyses also consider three other SLSNe-I, which have UV spectra before or near maximum light. The Gaia16apd *HST* spectra were taken with the similar setup as that of SN2017egm except G430L grating, and have been published in Yan et al. (2017). PTF12dam was observed with the *HST/WFC3* slitless grism G280 at -18.4 days before the peak, and $+44.2$ days after the explosion (Nicholl et al. 2013; Vreeswijk et al. 2017; Quimby et al. 2017). As shown in Table 2, PTF12dam has the longest time lag between the UV spectrum observation and the explosion date. Its near-UV *HST* spectrum reaches out to 1850Å and has a low resolution of 70 at 3000Å (Quimby et al. 2017). The iPTF13ajg spectrum was taken with X-shooter on the VLT telescope on 2013-04-17 at -4 days from the maximum light. With $z \sim 0.7$, this spectrum is the best quality near-UV spectrum taken with a ground-based telescope for a SLSN-I (Vreeswijk

et al. 2014).

To date, there are *HST* spectra for only five SLSNe-I, including SN2017egm, Gaia16apd, PTF12dam, PTF11rks and SN2011ke. The spectrum for SN2011ke is taken at late phase ($+24$ day post peak), and the data for PTF11rks has poor SNR (Quimby et al. 2017). This paper focuses on the pre-peak UV spectra, therefore, does not consider SN2011ke and PTF11rks data. Optical spectra of SLSNe-I at $z > 0.5$ from ground-based telescopes also reach the rest-frame UV. However, most spectra have low SNR and their continua are not well characterized. The exception is iPTF13ajg which has a high quality optical spectrum near the maximum light.

3. RESULTS

3.1. The Diversity and uniformity of SLSN-I UV spectra at maximum light

With these early-time UV spectra, we have two goals – (1) quantify SLSN-I spectral continuum and absorption feature variations, which is important for estimating bolometric corrections and for modeling light curves of SLSNe-I based on broad band optical photometry, (2) identify UV, especially far-UV, spectral features.

Figure 1 presents the *HST* spectrum of SN2017egm, in comparison with those of Gaia16apd, PTF12dam and iPTF13ajg. The spectra were corrected for the Galactic extinctions (Table 2) and arbitrarily scaled for visual clarity. The two example spectra in Figure 2 illustrate that the SLSN-I UV and optical continuum cannot be simultaneously fit by a blackbody with a single temperature. This finding was also noted by Chomiuk et al. 2011 for SLSN-I PS1-10ky at $z = 0.9$. These two figures together demonstrate that the difference in UV SED shape between Gaia16apd and iPTF13ajg can not be explained by the difference in blackbody temperature alone.

To characterize UV & optical spectral continuum, we use Markov Chain Monte Carlo (MCMC) method, specifically utilizing python emcee package (Foreman-Mackey et al. 2013). Our adopted model is a modified blackbody, defined as $f_{\lambda}(T) = (\lambda/\lambda_0)^{\beta} f_{\lambda, BB}(T)$ for $\lambda < \lambda_0$ and $f_{\lambda}(T) = f_{\lambda, BB}(T)$ for $\lambda > \lambda_0$. We do not use all of the pixels from the observed spectra and exclude the spectral regions with prominent broad absorption features. We resample the spectra by selecting a number of spectral regions (with width of 50 – 150Å) presenting the continuum, and compute the averaged flux density from each spectral bin. For example, the selected regions used for the MCMC calculations are shown as solid black points for SN2017egm in Figure 1, with each error bars in X-axis marking the selected regions.

Our model has four variables, T , λ_0 , β and $\log_{10}(A)$ (a scaling factor taking into account of distance). Table 3 shows the results from the computation where all four parameters are considered as variables. Figure 3 shows the probability distributions of these four variables calculated from the MCMC simulation for SN2017egm. We find that λ_0 values are similar, ~ 2800 Å, for the three SLSN-I, except Gaia16apd. As Table 3 shown, Gaia16apd has λ_0 at a longer wavelength. The derived UV power-law slope β is small, 0.51. This is not surprising because λ_0 and β have some degree of inter-dependency, larger λ_0 value would lead to smaller β . Therefore, to make a meaningful comparison of β values,

it makes more sense to fix λ_0 at 2800\AA and recompute the other three parameters. Table 4 shows the MCMC simulation results when considering only three variables, T , β and $\log_{10}(A)$. In the remaining of the paper and the relevant figures, we quote the T , β values derived from the MCMC calculations with the fixed λ_0 .

The spectral continua at $\lambda > 2800\text{\AA}$ can be well described by a blackbody with $T_{BB} \sim 17094^{+587}_{-285}$ K for SN2017egm, 16703^{+480}_{-398} K for Gaia16apd, and slightly cooler temperature of 15008^{+200}_{-75} K for iPTF13ajg and 14684^{+87}_{-76} K for PTF12dam. This value is smaller for iPTF13ajg than derived by Vreeswijk et al. (2014). The lower temperature for PTF12dam is consistent with the phase when the spectra were taken, when the ejecta has a longer time to cool.

At $\lambda < 2800\text{\AA}$, SLSN-I UV continuum is significantly below the blackbody model. The UV deviation from a blackbody emission (or UV continuum suppression) is well known for normal supernovae, and is generally thought due to a forest of line absorption by heavy elements (so called line blanketing at $\lambda < 1300\text{\AA}$) as well as UV photons scattered to longer wavelengths by the fast expanding ejecta (Pauldrach et al. 1996; Bufano et al. 2009). It is also known that at maximum light, SLSNe-I tend to be bluer and the UV continuum suppression is much less than that of normal SNe (Quimby et al. 2011; Yan et al. 2017).

Comparison of Table 4 suggests a robust conclusion that SN2017egm has $\beta = 0.8^{+0.15}_{-0.16}$, much smaller than $\beta = 2.94^{+0.09}_{-0.04}$ for iPTF13ajg. Another way of describing the UV continuum variation is the 1400\AA to 2800\AA continuum flux ratio, which changes from 1.5 in Gaia16apd, to 0.5 in iPTF13ajg. Nicholl et al. (2017c) also uses a modified blackbody SED with $\beta = 1$ to model a sample of SLSNe-I. Our analysis shows that the UV SED variation is large enough that a single SED template is not sufficient when modeling samples of SLSNe-I. The large near-UV SED variation is also noted in Lunnan et al. (2017), which found that for a sample of SLSNe-I at $z \sim 0.5 - 1.5$, their peak absolute magnitudes at near-UV (2600\AA) span over 4 magnitudes, whereas the peak magnitudes at 4000\AA spread over only 2 magnitudes.

The physical origin of the UV variation in SLSNe-I is not clearly understood. Nicholl et al. (2017b) has argued that the extremely high UV continuum at maximum light from Gaia16apd could be explained by its high magnetar power and the small photospheric radius. In Figure 4, we plot the magnetar power as a function of time since explosion, described by the equations:

$$t_{spin} = 1.3 \times 10^5 \left(\frac{M_{NS}}{1.4M_{\odot}} \right)^{3/2} \left(\frac{B}{10^{14}G} \right)^{-2} \left(\frac{P}{1ms} \right)^2 \text{ s}$$

$$F_{mag} = 2 \times 10^{47} \left(\frac{B}{10^{14}G} \right)^2 \left(\frac{P}{1ms} \right)^{-4} \left(1.0 + \frac{t}{t_{spin}} \right)^{-2} \text{ erg/s}$$

We choose the time since explosion because it is directly related to ejecta cooling, thus the appearance of the observed spectra. We adopt the magnetar model parameters for these four events from Nicholl et al. (2017c, Appendix A), derived using *MOSFiT* (Guillochon et al. 2017). At the time of the spectral observations (verti-

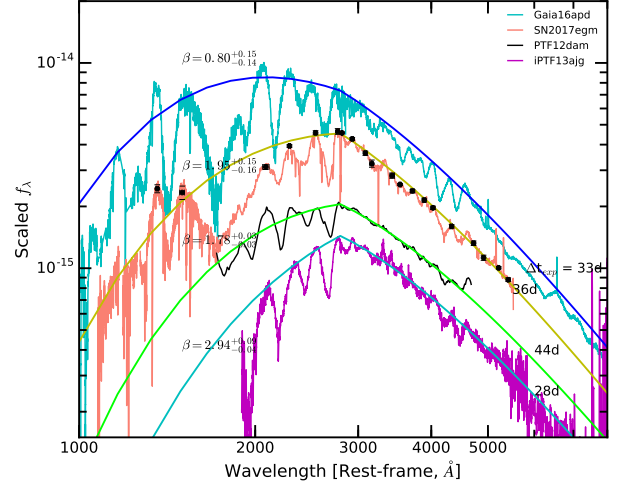


FIG. 1.— The UV spectra of four low- z SLSNe-I. The Y-axis is flux density in $\text{erg/s/cm}^2/\text{\AA}$. The spectra are scaled to offset them from each other for visual clarity. We also show one example of how we select spectral regions (solid black points for SN2017egm) as the input to the MCMC calculation. MCMC model fits to the continua are overlaid based on the parameters derived from the MCMC calculations with the fixed λ_0 and listed in Table 4.

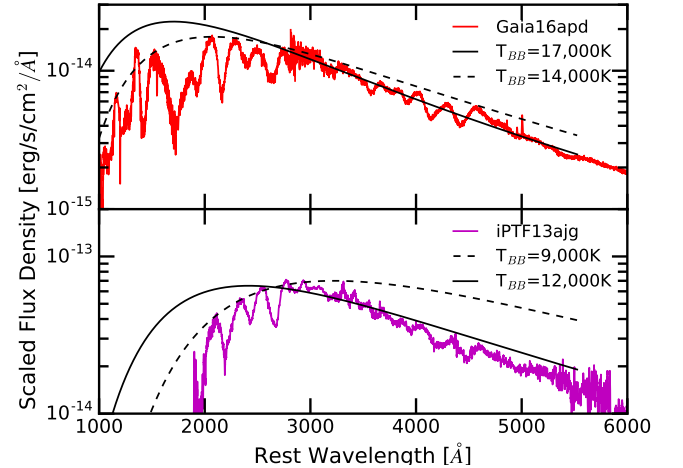


FIG. 2.— The plot shows that a pure blackbody function can not fit the observed spectra.

cal line in Figure 4), iPTF13ajg has the most powerful heating source F_{mag} , but its far-UV continuum is the most suppressed. This implies that magnetar power is not directly proportional to UV continuum emission. Nicholl et al. (2017c) noted that photospheric radius R may play an important role, in addition to the magnetar power. However, we note that the regions producing far-UV continuum photons might not be the same as the photospheric surface, which is usually determined by assuming color temperature T_{BB} equals to effective temperature T_{eff} , defined as $L_{bol} = 4\pi\sigma R^2 T_{eff}^4$ (see discussion below). The significant deviation from a single blackbody fit at the UV wavelength appears to support the idea that UV photons may come from different regions than that of optical photons. Therefore, we need a better understanding of the radiative physics of early-

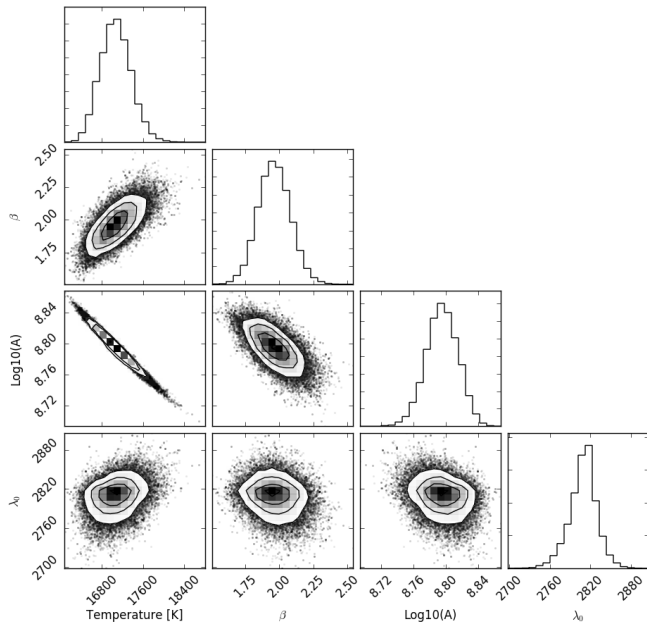


FIG. 3.— The probability distributions of the four variables (T , β , λ_0 and $\log_{10}(A)$) derived from the MCMC simulations for SN2017egm.

time SLSN-I spectra.

Quimby et al. (2017) carried out a detailed analysis of near-UV spectra of 8 SLSNe-I. They identified three common features at 2200, 2450 and 2650Å, likely produced by C II, C III, Ti III, Mg II and Mn II (Also see Howell et al. 2013; Mazzali et al. 2016; Dessart et al. 2012). Here we focus on the far-UV, and plot out the normalized spectra in Figure 5, where the top panel shows the far-UV spectra from 1000 - 3000Å, and the bottom panel shows the optical portion between 3000 - 5000Å. To align the spectral features, we redshifted the spectra by the respective amount indicated in the figure. The shifts are different for UV and optical spectra of the same object. We used the local continuum to normalize each spectrum. Because velocities for PTF12dam are well measured in Quimby et al. (2017), we shift other spectra relative to PTF12dam in order to get estimates of the velocities. In the optical, we align all spectra by O II absorption at 4200Å (feature B, Quimby et al. 2017), and in the UV, we align the spectra by the three near-UV features. Figure 5 also includes the synthetic spectrum (blue dashed line) generated by syn++ model (Thomas et al. 2011) and presented in Quimby et al. (2017).

With the first epoch *HST* spectrum at $\Delta t_{exp} = +44.2$ day, PTF12dam has an O II velocity of $\sim 10,000 \text{ km s}^{-1}$. From the comparison, SN2017egm and iPTF13ajg have the same O II velocities, but at earlier phases ($\Delta t_{exp} = 36$ & 28 d respectively). Gaia16apd is different, has a much higher velocity, $\sim 14,500 \text{ km s}^{-1}$ at the maximum light ($\Delta t_{exp} = 33$ d), consistent with what we derived in Yan et al. (2017). In addition, the UV spectral comparison appears to give different results. Gaia16apd, SN2017egm and iPTF13ajg are +6,000, +2,000, +2,000 km s^{-1} faster than PTF12dam respectively. This implies that far-UV spectral formation layers are moving faster than the O II ions which produce the absorption series at 3500 - 4700Å.

In the published literature on SLSNe-I, it is commonly assumed that blackbody temperature T_{BB} (also called color temperature) is the same as photospheric effective temperature (not directly observed) T_{eff} , defined as $L_{bol} = 4\pi\sigma R^2 T_{eff}^4$. Using this equation, we can infer photospheric radius R as well as photospheric velocity $v_{phot} = R/\Delta t_{exp}$, here Δt_{exp} is the time since explosion. We find the ratio v_{phot}/v_{OII} of 0.49, 0.51, 1 and 0.62 for Gaia16apd, SN2017egm, iPTF13ajg and PTF12dam respectively. Only iPTF13ajg appears to have O II velocity close to its photospheric velocity, and other three events with less UV suppression seem to have O II ions expanding faster than photosphere. One might argue the small photospheric velocities could be due to uncertainties in Δt_{exp} . It seems unlikely that for all three events Δt_{exp} values are systematically over-estimated by a factor of 2, which would make the true rise times for Gaia16apd and SN2017egm ~ 15 days. This is too short for a SLSN-I (Nicholl et al. 2015; De Cia et al. 2017b), making this explanation unlikely. Another possibility is that the assumption of $T_{BB} = T_{eff}$ is no longer valid, with $T_{eff} \leq T_{BB}$, which would imply larger photospheric radius R and v_{phot} . As discussed in Nakar & Sari (2010), T_{eff} in $L_{bol} = 4\pi\sigma R^2 T_{eff}^4$ is based on the assumption of thermal equilibrium. The observed temperature T_{BB} is mostly determined by the outer layers of ejecta. If these layers are not in thermal equilibrium, the observed temperature T_{BB} would be $> T_{eff}$. We conclude that the high velocity gas layers which make significant contributions to the observed spectra for Gaia16apd, SN2017egm and PTF12dam are likely not in thermal equilibrium.

The far-UV *HST* spectra show three new absorption features at 1250, 1400 and 1650Å, detected in both SN2017egm and Gaia16apd (also partially in PTF12dam), and with similar equivalent widths. We note that the 1650Å feature is particularly broad and strong. We use the synthetic spectrum to make a tentative spectral identifications. The mock spectrum includes ions such as Fe III, Ti III, Ti II, Si II, Mg II, O II, O I, C IV, C III and C II, and the detailed discussion can be found in Quimby et al. (2017). We identified the 1250Å feature as the blend of C II, O I, Si II, Ti III and Fe III, and the 1400Å feature from C IV, Si II and Ti III. However, the most prominent absorption at 1650Å is poorly explained by the synthetic spectrum. This feature blends into the absorption at 1950Å which was identified as Fe III, and possibly also Co III (Mazzali et al. 2016). It is possible that the broad feature at 1650Å is a blend of Si II, C II, C III and Fe III, with strength and broadening significantly different from the syn++ calculated spectrum. Better line identifications at the far-UV are needed in future studies.

In summary, the seven broad UV absorption features are stronger than the features in the optical regime in the early-time spectra of SLSNe-I. We find that their strengths, *i.e.* equivalent widths, appear to be remarkably similar within a factor of two among these four events. This was also noted in Nicholl et al. (2017b) for Gaia16apd and iPTF13ajg. The uniformity and large equivalent width of UV spectral absorption features bode well for high- z SLSN-I searches since ground-based follow-up spectroscopy will rely on them for solid classifications.

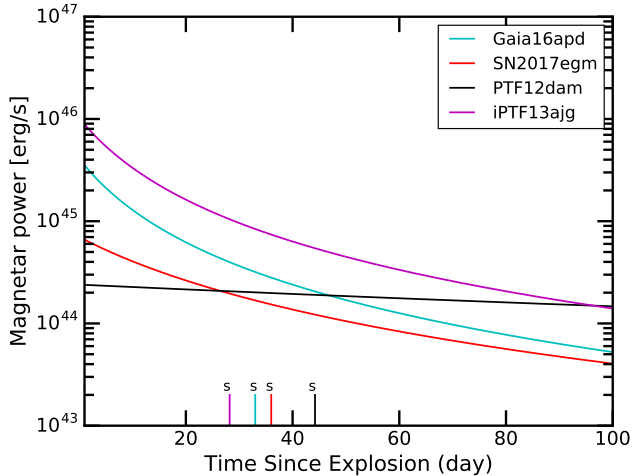


FIG. 4.— The magnetar power for each event in our sample. The magnetar model parameters for these four events are taken from Nicholl et al. (2017b).

3.2. Interstellar and circumgalactic media along the line-of-sight to SN2017egm

The far-UV spectrum of SN2017egm provides a sensitive probe of ISM absorbers at different velocities along the line-of-sight and enables the measurements of metal abundances, thus shedding light on the SN host environment.

We first applied a Savitsky-Golay filter to the SN spectrum to produce a model of the complex continuum emission, including the broad SN features. Strong narrow lines were interpolated over prior to applying the filter. We then divided the observed spectrum by the model spectrum to produce a normalized spectrum, shown in Figure 6. This spectrum clearly reveals several sets of absorption systems: one at $z = 0$ from the Milky Way Galaxy, and two more related to the host system. The first, at $z = 0.0307$, is effectively consistent with the emission-line redshift of NGC 3191. The other system is at $z = 0.0299$, corresponding to a relative blue-shift of 235 km s^{-1} .

Although there is no other galaxy directly along the line of sight towards NGC 3191, at $73''$ to the west (44 kpc in projection) a companion galaxy, SDSSJ101857.98+462714.6, is visible. The spectroscopic redshift of this system is $z = 0.02993$: consistent with our second absorption system, making this galaxy a plausible counterpart of that system. Alternatively, the blue-shifted system could be due to an outflow or wind emanating from NGC 3191, as has been seen in some other high-SFR low- z galaxies (Grimes et al. 2009; Heckman et al. 2015; Alexandroff et al. 2015).

Our spectroscopic coverage includes the damped Lyman- α absorption (DLA) feature from neutral hydrogen. Analysis of this feature is complicated by blending between the host and the companion, as well as uncertainties in the continuum modeling, and it is difficult to constrain the individual contributions of the two component systems to the overall line. Modeling the line as two separate, blended Voigt profiles, we can robustly constrain the total column density of the two systems together to $5 \times 10^{19} \text{ cm}^{-2} \leq N(\text{HI}) \leq 9 \times 10^{19} \text{ cm}^{-2}$; our best-fit estimate is $(6.7 \pm 1.2) \times 10^{19} \text{ cm}^{-2}$, making

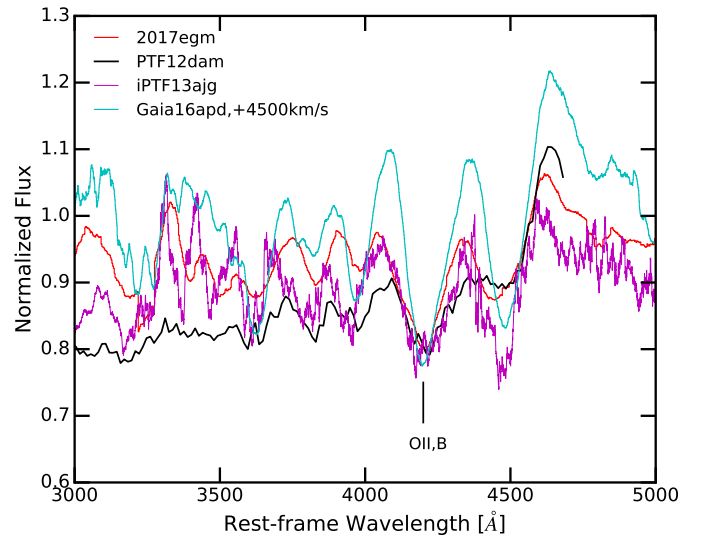
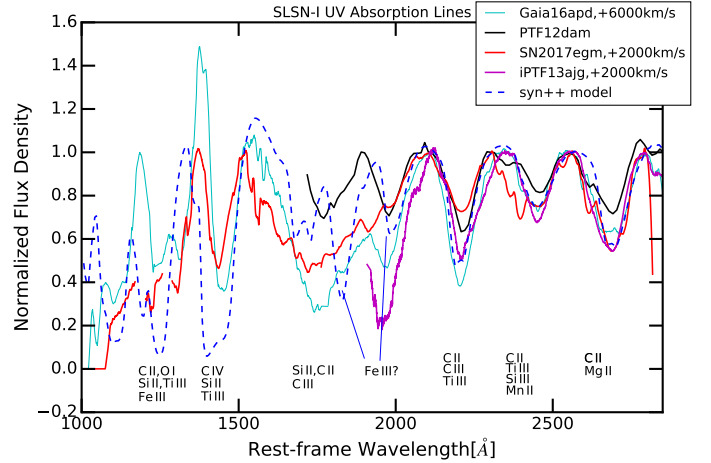


FIG. 5.— The normalized spectra in comparison with the model spectrum (blue dashed line) generated by Quimby et al. (2017) using syn++ code (Thomas et al. 2011). To align the spectral features, we redshifted the spectra by the indicated velocities. The shifts are generally different for UV and optical spectra for the same SLSN-I.

the system technically a sub-DLA (Péroux et al. 2003). This spread in $N(\text{HI})$ is due to uncertainties in the relative contributions of the two systems and continuum placement. The derived $N(\text{HI})$ is an order of magnitude less than a typical value through a disk of a spiral galaxy with stellar mass $> 10^{10} M_{\odot}$, measured by The HI Nearby Galaxy Survey (THINGS) (Walter et al. 2008; Leroy et al. 2008). This result has two implications. One is that SN2017egm may have exploded on the near side of the galaxy, where there is less neutral HI material along the line-of-sight. One may argue for the second possibility that UV fluxes from the SN explosion could photo-ionize a large fraction of neutral HI in the disk of NGC 3191, and SN2017egm could be anywhere in the disk. To validate this hypothesis, we calculate the time required, t_{phot} , to photo-ionize $N(\text{HI}) \sim 10^{21} \text{ cm}^{-2}$ over a scale height R of an HI disk. HI-ionizing flux, J_{UV} at the time of SN explosion is poorly constrained by observation. Let us take J_{UV} as a fraction of f_{UV} of the peak bolometric luminosity (L_{bol}), we have $J_{\text{UV}} = \frac{f_{\text{UV}} L_{\text{bol}}}{4\pi R^2 (13.6 \text{ eV})}$.

The Milky Way thin disk (stellar) has a scale height of 100 pc^1 . As the most conservative assumption, let us take $R = 50 \text{ pc}$ if the SN is at the mid-plane, we have $J_{UV} = 3 \times 10^{11} (f_{UV}/0.01) \text{ cm}^{-2} \text{ s}^{-1}$. In this equation, without any knowledge of the early-time UV fluxes from SN2017egm, we assume it is only 10% of the estimated bolometric luminosity ($f_{UV} = 0.01$). Here the maximum L_{bol} is $2 \times 10^{44} \text{ erg s}^{-1}$. To photo-ionize a column of 10^{21} cm^{-2} HI atoms, we need the same number of HI ionizing photons, thus, over a time scale of t_{phot} , we have $J_{UV} t_{phot} \simeq 10^{21} \text{ cm}^{-2}$, leading to $t_{phot} = 3 \times 10^9$ second. This is two orders of magnitude longer than the time lag between the explosion and the *HST* spectroscopy date for SN2017egm. Since $t_{phot} \propto R^2 f_{UV}^{-1}$, a larger f_{UV} value will shorten the photoionization time scale t_{phot} by a factor of a few, but not sufficient to change our conclusion. This result suggests that photo-ionization due to the SN explosion is probably localized within a 5 pc region.

Using the calibrated relation of $N(\text{HI}) = 6.86 \times 10^{21} \times E(B-V)$ (Güver & Özel 2009), we derive $E(B-V)$, the host dust extinction of 0.007. This relation is based on Galactic dust-to-gas and dust-to-metal ratios and should work reasonable well for galaxies with high metallicities. The $E(B-V) = 0.3$ (Chen et al. 2017b; Izzo et al. 2017), derived from nebular emission lines at the SN location, represents the dust extinction through the full disk of NGC3191. The low host extinction correction is further supported by the fact that the blackbody temperature derived from the uncorrected SN2017egm spectra appears to be consistent with that of other SLSNe-I in dwarf galaxies.

Detailed abundance analysis of the metal lines is complicated by the relatively low resolution ($\text{FWHM} \sim 0.47 \text{ \AA} \sim 120 \text{ km s}^{-1}$) of the COS G140L grating, which means that most lines strong enough to detect are also saturated. Additional continuum normalization uncertainties and S/N limitations impose other uncertainties. If a line is saturated, its equivalent width, *i.e.* line strength, becomes less sensitive to column density of the corresponding ion, making abundance measurement unreliable. Si II 1190, 1193, 1526Å lines are strong lines and commonly used for metallicity measurements, however, they are saturated in our data. This is validated by checking their equivalent widths, which are not proportional to their oscillator strengths for the same ion column density.

Three weaker lines, S II $\lambda\lambda 1250, 1253 \text{ \AA}$, Fe II $\lambda 1608 \text{ \AA}$ and Al II $\lambda 1670 \text{ \AA}$ are not saturated and offer a more promising route to constrain the abundances. They are weak but still significant detected. In the optically thin regime, the column density $N(\text{X})$ of an ion X is directly proportion to line strength, with $N(\text{X}) = \tau [m_e c^2 / (\pi e^2 f \lambda^2)]$, and τ is the integrated optical depth over a whole line, f is the oscillator strength, m_e , e and c are electron mass, electron charge and speed of light respectively. τ is computed from the following equation, $\tau(\lambda) = [A / (\sqrt{2\pi} b_D)] \exp[-(\lambda - \lambda_0)^2 / (2b_D^2)]$, with A the integrated line flux, b_D is the line width and the derived line profile is $flux(\lambda) = \exp[-\tau(\lambda)]$. As illustrated by the equation, the optical depth profile is a Gaussian and the line profile is an exponential. The ob-

served line profile is the convolution product of the exponential profile with the instrument Line-Spread-Function (LSF). Line width b_D is intrinsic line width. We explored various fitting parameters and find that the b_D values of 0.4 and 0.2Å achieve reasonably good fits to all of the absorption lines.

Table 5 listed the column densities and abundances for the metal lines at these two velocities. Figure 7 shows the fits to various metal lines and broad Lyman- α absorption. The best fit to Lyman- α requires two almost equal strength absorption components with a velocity separation of 235 km s^{-1} . The χ^2 values from the fits suggest that the probability of Lyman- α being a single line at one redshift is very small, $< 2\%$. The derived HI column densities are $(3.0 \pm 0.8) \times 10^{19}$ and $(3.7 \pm 0.9) \times 10^{19} \text{ cm}^{-2}$ for the two absorbers at $z = 0.0307$ (redshift of NGC3191) and 0.0299 (companion galaxy) respectively. Element abundance $[X/H]$ is calculated as $[X/H] = 12 + \log_{10}(N(\text{X})/N(\text{HI})) - [X/H]_{\odot}$, and the corresponding error considers both $N(\text{X})$ and $N(\text{HI})$ errors quadratically. In Table 5, $[X/H]_{\text{obs}}$ indicates the abundance values computed directly from the column densities without any other corrections. We find $[S/H]_{\text{obs}}$ of 0.30 and 0.38 (2.0 & $2.4 Z_{\odot}$) for the two velocity component respectively.

There are several effects to consider. One is ionization correction which accounts for the fact that some H and S atoms are ionized². Ionization correction for H is adopted from a *HST* UV spectroscopy study of a sample nearby sub-DLAs by Werk et al. (2014). We adopt H ionization fraction of 72% at the corresponding HI column density of $6.7 \times 10^{19} \text{ cm}^{-2}$ (Werk et al. 2014, Table 1). Ionization correction for S is much more difficult and is not considered here. Even without this correction, the $[X/H]_{\text{HC}}$ including H ionization correction should serve meaningful constraints on the lower limits to the abundances. We conclude that $[S/H]$ abundance should be greater than $[S/H]_{\text{HC}} \sim 0.06$ and 0.14 for the two velocity components respectively (1.15 and 1.4 Z_{\odot} , Table 5).

Another effect to consider is dust depletion of S, Fe and Al, which reduces the strengths of the absorption lines. This is why the observed $[\text{Fe}/\text{H}]_{\text{obs}}$ values are very low, -0.62 and -1.36 . The large observed $[\text{S}/\text{Fe}]_{\text{obs}}$ and $[\text{S}/\text{Fe}]_{\text{obs}}$ unambiguously imply a substantial amount of dust, comparable to that of the Milky Way. Although dust depletion correction to metal elements are uncertain, we proceed and adopt the method based on $[\text{S}/\text{Fe}]$ ratio and described in De Cia et al. (2016, 2017). We derived the dust depletion corrected $[\text{Fe}/\text{H}]_{\text{DC}}$ ratios of 0.48 and 1.10 (3 and 12 Z_{\odot}). Including both the dust depletion and H ionization corrections, the final $[\text{Fe}/\text{H}]_{\text{corr}}$ values are 0.25 & 0.87 (1.8 and 7.4 Z_{\odot}) for the two velocity components.

After both H ionization and dust depletion corrections, S, Fe and Al abundances at $z = 0.03070$ and 0.0299 are all super-solar, except $[\text{Al}/\text{H}]$ at $z = 0.0307$, which is -0.25 (0.56 Z_{\odot}). All six metal abundance values indicate a wide range of metallicities for the two absorbers. Such a wide range reflects the difficulties of this type of measurements using absorption lines from a moderate resolution spectrum. If we take the average value of the derived abundances, the result is clearly above so-

¹ the HI gas can be more extended (Marasco & Fraternali 2011)

² H and S ionization potentials are 13.6 and 23 eV respectively.

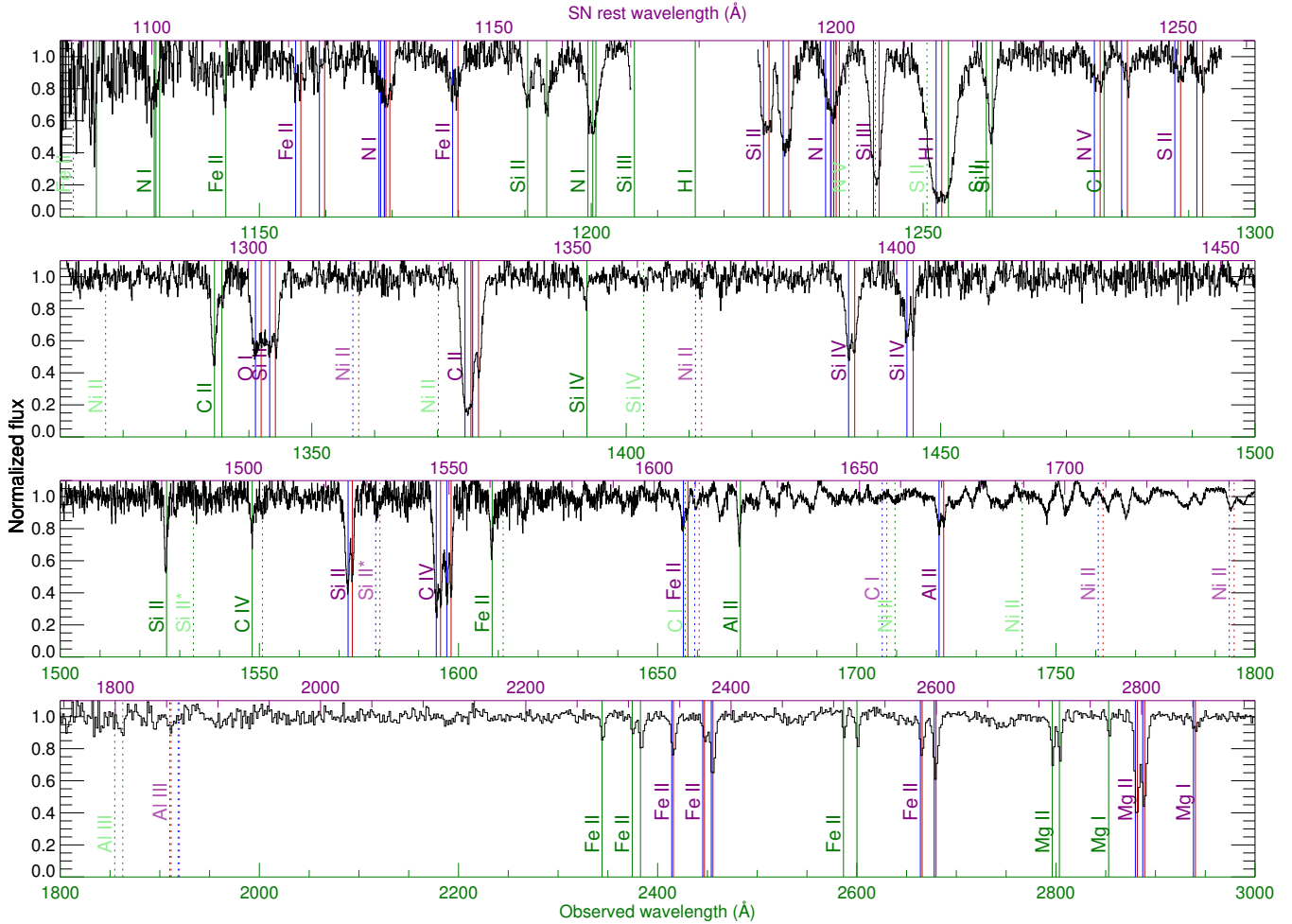


FIG. 6.— *HST* COS and STIS spectra of SN 2017egm after normalization of the continuum using Savitsky-Golay convolution. Absorption lines originating from the Milky Way Galaxy are marked as green, while lines from the host system are marked as red (host component) or blue (companion component) and jointly labeled with purple text. Dotted lines and lighter text colours indicate notable nondetections or marginal detections. The resolution in the mid-UV (bottom-most panel) is not sufficient to resolve the two velocity components in the host system.

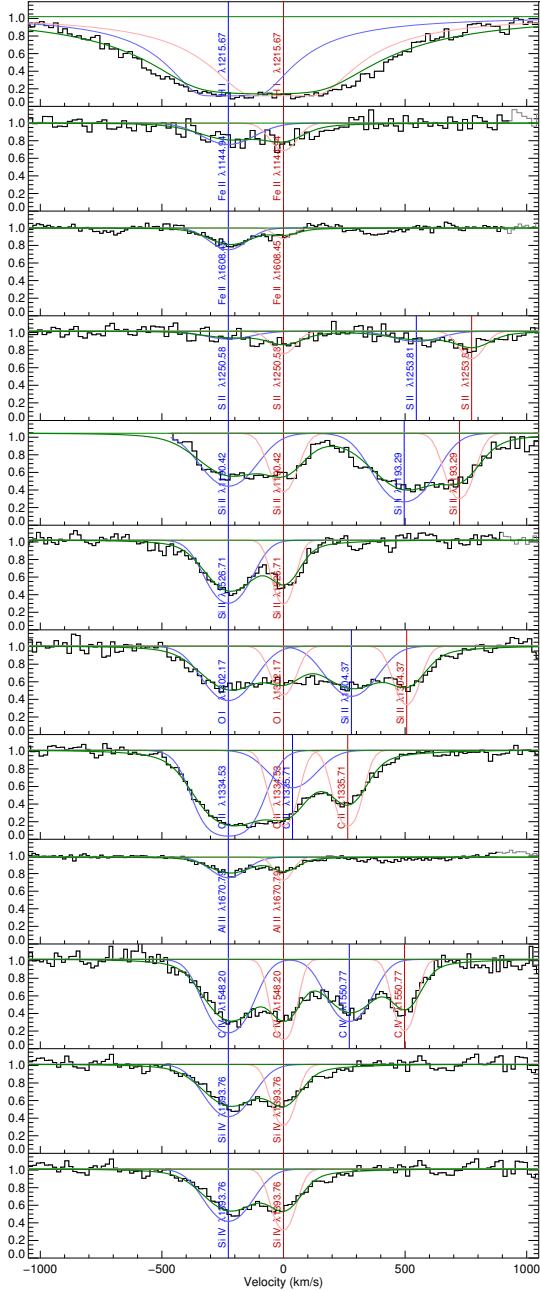


FIG. 7.— Profiles of prominent absorption lines from various species associated with the host-galaxy system of SN 2017egm (see also Figure 6). All lines except for the sub-DLA (top plot) show a bimodal profile, with the red component at a redshift matching that of NGC 3191 and the bluer component (-235 km s^{-1}) at the exact redshift of the companion galaxy SDSSJ101857.98+462714.6. Red and blue curves show modeled intrinsic profiles and the green curves are the combined results after convolution with the COS instrumental line-spread-function (LSF).

lar metallicity. Therefore, taking together the six metal abundance measurements, we conclude that the environment of SN2017egm likely has a solar or higher metallicity. For comparison, the median metallicity of 40 SLSN-I host galaxies published in the literature is $0.3Z_{\odot}$ on the PP04 N2 scale (Pettini & Pagel 2004; Chen et al. 2017b). Both nebular emission line and UV absorption line analyses indicate that the metallicities at the SN location and the companion galaxy are at least a factor of 3 higher

than that of the host galaxies of most SLSNe-I at low redshift.

Considering the low HI column density alone, one might argue that there could be a dwarf companion galaxy at the location of SN2017egm. However, the high metallicity result makes this scenario very unlikely since dwarf galaxies tend to be metal poor.

4. SUMMARY

We present the maximum light *HST* UV & optical spectra of the closest SLSN-I, a rare event exploded in a massive spiral galaxy. Using this data, together with three other SLSNe-I, we address the question of how early-time UV continuum and spectral features of SLSN-I vary from source to source. In addition, we set constraints on the metal abundances of local environment of SN2017egm by performing a detailed analysis of narrow UV absorption lines detected in the *HST* spectra.

High quality early-time UV spectra of four SLSNe-I appear to detect a common set of broad UV absorption features (seven) between $1000 - 2800 \text{ \AA}$. And the three features at the far-UV $1000 - 1500 \text{ \AA}$ are new, revealed only by the *HST* data for SN2017egm and Gaia16apd (Yan et al. 2017). These UV features appear to be much stronger than ones in the optical regime at similar phases. And furthermore, their absorption strengths characterized by their equivalent widths are similar within a factor of 2 from source to source. The physical implication of this result is worth further exploring in the future. It should provide data constraints on spectral formation models for SLSN-I, which will help us better understand the characteristics of outer photospheres of SLSN-I at pre-peak phases. These results also bode well for optical spectral classification of SLSN-I candidates at $z > 2$.

In contrast to the uniformity of the UV absorption features, the $1000 - 3000 \text{ \AA}$ continua vary significantly. We quantify the UV continuum variation by using a modified blackbody function, $f(T_{BB}, \lambda) = B(T_{BB}, \lambda)(\lambda/\lambda_0)^\beta$ for $\lambda < \lambda_0$, and $f(T_{BB}, \lambda) = B(T_{BB}, \lambda)$ for $\lambda > \lambda_0$. If considering T , β and λ_0 all as the variables, our MCMC calculations find that SN2017egm, iPTF13ajg and PTF12dam all have $\lambda_0 \sim 2800 \text{ \AA}$. Since β and λ_0 have some degrees of inter-dependency, in order to compare the far-UV continuum slopes, we fix λ_0 at 2800 \AA for all four SLSN-I. The MCMC calculations find that the parameter β , describing the decline of the far-UV continuum toward the shorter wavelength, is $0.80^{+0.15}_{-0.16}$, $1.96^{+0.15}_{-0.14}$, $1.78^{+0.03}_{-0.03}$ and $2.94^{+0.09}_{-0.04}$ for Gaia16apd, SN2017egm, PTF12dam and iPTF13ajg respectively. Our SED model is useful for calculating bolometric corrections and modeling of light curves using only optical photometry. Using PTF12dam as the reference, we find Gaia16apd has the highest velocity, $14,500 - 16,000 \text{ km s}^{-1}$, and the ionized gas producing UV spectral features are clearly moving faster than that of O⁺ ions forming O II absorption at $3500 - 4700 \text{ \AA}$.

We find the observed parameters such T_{BB} and v_{OII} can not be consistently related to the photospheric temperature and velocity T_{eff} and v_{phot} where $T_{eff} = (L_{bol}/4\pi\sigma(v_{phot}\Delta t_{exp})^2)^{1/4}$. This suggests that the ejecta layers producing continuum emission (photosphere) and absorption features are probably not in thermal equilibrium and their expansion speeds are likely different.

The *HST* SN2017egm spectra also detect a rich set of narrow absorption lines produced by gas absorbers along the line-of-sight³. Our medium resolution far-UV spectra (FWHM \sim 120 km s⁻¹) clearly detected and resolved two sets of absorption systems, with one component matching the redshift of the host galaxy NGC 3191, and the second, 235 km s⁻¹ blue shifted component, consistent with the redshift of the companion galaxy, SDSSJ101857.98+462714.6 (45 kpc away). We hypothesize that these two galaxies are undergoing tidal interaction, and the two absorption systems originate from halo gas surrounding each galaxy.

Besides narrow metal absorption lines, our data also detected a Lyman- α absorption from the host galaxy with a total column density of $(6.7 \pm 1.2) \times 10^{19}$ cm⁻² (sub-DLA) This is an order of magnitude smaller than the typical HI column density (10^{21} cm⁻¹) measured in the disks of nearby spiral galaxies by the THINGS survey (Walter et al. 2008; Leroy et al. 2008), suggesting that SN2017egm is likely to be on the near side of the galaxy, with a fairly low extinction ($E(B - V) = 0.007$) for the supernova.

Although medium spectral resolution prevents us from

accurate measurements of metal abundances of interstellar and circumstellar gas, we are able to set the probable lower limits to metallicities of the two velocity components to $> 1 Z_{\odot}$. This is consistent with nebular gas-phase metallicities measured from optical spectra at the SN location (IFU data) and the companion galaxy (SDSS) (Nicholl et al. 2017a; Bose et al. 2017; Chen et al. 2017b; Izzo et al. 2017). Combining the low HI column density result with the high metallicity measurement, we can rule out the scenario where SN2017egm is located in a dwarf companion galaxy. We conclude that although it is rare, a SLSN-I event can explode in a metal rich environment.

We acknowledge many useful discussions with Matt Nicholl at Harvard and Janet Chen at Max-Planck-Institut für Extraterrestrische Physik, in Germany on the measurements of gas-phase metallicities in NGC3191 and the companion galaxy. We thank Nadia Blagorodnova for providing example python emcee scripts for our spectral fitting. We also thank Nick Scoville at Caltech for discussions on the HI column density distribution of nearby galaxies.

Facilities: HST.

Software: Python, Astropy

REFERENCES

- Alexandroff, R. M., Heckman, T. M., Borthakur, S., Overzier, R., & Leitherer, C. 2015, *ApJ*, 810, 104
- Asplund, M., Grevesse, N., Sauval, A. J., & Scott, P. 2009, *ARA&A*, 47, 481
- Bose, S., Dong, S., Pastorello, A., et al. 2017, ArXiv e-prints, arXiv:1708.00864 [astro-ph.HE]
- Bufano, F., Immler, S., Turatto, M., et al. 2009, *ApJ*, 700, 1456
- Chen, T.-W., Smartt, S. J., Yates, R. M., et al. 2017a, *MNRAS*, 470, 3566
- Chen, T.-W., Schady, P., Xiao, L., et al. 2017b, ArXiv e-prints, arXiv:1708.04618
- Chomiuk, L., Chornock, R., Soderberg, A. M., et al. 2011, *ApJ*, 743, 114
- De Cia, A., Ledoux, C., Mattsson, L., et al. 2016, *A&A*, 596, A97
- De Cia, A., Ledoux, C., Petitjean, P., & Savaglio, S. 2017, ArXiv e-prints, arXiv:1709.06578
- De Cia, A., Gal-Yam, A., Rubin, A., et al. 2017, arXiv:1708.01623
- Delgado, A., Harrison, D., Hodgkin, S., et al. 2017, *Transient Name Server Discovery Report*, 591
- Dessart, L., Hillier, D. J., Waldman, R., Livne, E., & Blondin, S. 2012, *MNRAS*, 426, L76
- Dong, S., Bose, S., Chen, P., et al. 2017, *The Astronomer's Telegram*, 1049
- Foreman-Mackey, D., Hogg, D. W., Lang, D., & Goodman, J. 2013, *PASP*, 125, 306
- Gaia Collaboration, Prusti, T., de Bruijne, J. H. J., et al. 2016, *A&A*, 595, A1
- Grimes, J. P., Heckman, T., Aloisi, A., et al. 2009, *ApJS*, 181, 272
- Guillochon, J., Parrent, J., Kelley, L. Z., & Margutti, R. 2017, *ApJ*, 835, 64
- Güver, T., & Özel, F. 2009, *MNRAS*, 400, 2050
- Heckman, T. M., Alexandroff, R. M., Borthakur, S., Overzier, R., & Leitherer, C. 2015, *ApJ*, 809, 147
- Howell, D. A., Kasen, D., Lidman, C., et al. 2013, *ApJ*, 779, 98
- Izzo, L., Thöne, C. C., García-Benito, R., et al. 2017, ArXiv e-prints, arXiv:1708.03856 [astro-ph.HE]
- Leloudas, G., Schulze, S., Krühler, T., et al. 2015, *MNRAS*, 449, 917
- Leroy, A. K., Walter, F., Brinks, E., et al. 2008, *AJ*, 136, 2782
- Lunnan, R., Chornock, R., Berger, E., et al. 2014, *ApJ*, 787, 138
- . 2017, ArXiv e-prints, arXiv:1708.01619 [astro-ph.HE]
- Marasco, A., & Fraternali, F. 2011, *A&A*, 525, A134
- Mazzali, P. A., Sullivan, M., Pian, E., Greiner, J., & Kann, D. A. 2016, *MNRAS*, 458, 3455
- Nakar, E., & Sari, R. 2010, *ApJ*, 725, 904
- Nicholl, M., Smartt, S. J., Jerkstrand, A., et al. 2013, *Nature*, 502, 346
- Nicholl, M., Smartt, S. J., Jerkstrand, A., et al. 2015, *MNRAS*, 452, 3869
- Nicholl, M., Berger, E., Margutti, R., et al. 2017a, ArXiv e-prints, arXiv:1706.08517 [astro-ph.HE]
- Nicholl, M., Guillochon, J., & Berger, E. 2017c, ArXiv e-prints, arXiv:1706.00825 [astro-ph.HE]
- . 2017b, *ApJ*, 835, L8
- Pauldrach, A. W. A., Duschinger, M., Mazzali, P. A., et al. 1996, *A&A*, 312, 525
- Perley, D. A., Quimby, R. M., Yan, L., et al. 2016, *ApJ*, 830, 13
- Péroux, C., Dessauges-Zavadsky, M., D'Odorico, S., Kim, T.-S., & McMahon, R. G. 2003, *MNRAS*, 345, 480
- Pettini, M., & Pagel, B. E. J. 2004, *MNRAS*, 348, L59
- Quimby, R. M., Kulkarni, S. R., Kasliwal, M. M., et al. 2011, *Nature*, 474, 487
- Schulze, S., Krühler, T., Leloudas, G., et al. 2016, ArXiv e-prints, arXiv:1612.05978
- Thomas, R. C., Nugent, P. E., & Meza, J. C. 2011, *PASP*, 123, 237
- Vreeswijk, P. M., Savaglio, S., Gal-Yam, A., et al. 2014, *ApJ*, 797, 24
- Vreeswijk, P. M., Leloudas, G., Gal-Yam, A., et al. 2017, *ApJ*, 835, 58
- Walter, F., Brinks, E., de Blok, W. J. G., et al. 2008, *AJ*, 136, 2563
- Werk, J. K., Prochaska, J. X., Tumlinson, J., et al. 2014, *ApJ*, 792, 8
- Yan, L., Quimby, R., Gal-Yam, A., et al. 2017, *ApJ*, 840, 57

³ Some features are visible in our Gaia16apd spectrum as well, but the features are weaker and the overall S/N is lower, preventing

reliable chemical analysis.

TABLE 1
HST/UV SPECTROSCOPY OBSERVATION LOG

Obs.UT	Name	Exp.Time	Instrument	Grating Å	$\Delta\lambda$	Spec Resolution	Obs.setup
2017-06-23	SN2017egm	7488.9	COS/FUV ^a	G140L	1118 - 2251	1500-4000	Seg-A/Time-TAG
2017-06-23	SN2017egm	1681.2	STIS/NUV	G230L	1570 - 3180	500-1010	NUV-MAMA
2017-06-23	SN2017egm	300.0	STIS/NUV	G430L	2900 - 5700	500-1010	NUV-MAMA
2012-06-02	Gaia16apd	4889	COS/FUV	G140L	1118 - 2251	1500-4000	Seg-A/Time-TAG
2016-06-02	Gaia16apd	2327	STIS/NUV	G230L	1570 - 3180	500-1010	NUV-MAMA
2012-05-26	PTF12dam	2448	WFC3/UVIS	G280	1840 - 4500	70 @3000Å	UVIS

^a COS/FUV data was taken using only Segment A.

TABLE 2
 PHASE INFORMATION FOR THE FOUR SLSNE-I

Name	Redshift	Spec.Date Day	Peak Date Day	Exp. Date Day	Δt_{exp} Day
SN2017egm	0.03	57927	57924	57890	35.9
Gaia16apd	0.1018	57541	57541	57505	32.7
PTF12dam	0.1078	56073	56096.7	56020.9	47
iPTF13ajg	0.7403	56399	56405	56350	28.2

TABLE 3
 RESULTS FROM THE MCMC SIMULATION - VARIABLE λ_0

Obj.	T K	β	λ_0	$\log_{10}(A)$
SN2017egm	17095 ⁺⁴⁶² ₋₁₉₃	1.95 ^{+0.10} _{-0.09}	2817.5 ⁺⁷⁸ ₋₁₀	8.79 ^{+0.02} _{-0.01}
Gaia16apd	17403 ⁺³¹³¹ ₋₆₄₇	0.51 ^{+0.4} _{-0.16}	3133 ⁺⁴⁵³ ₋₅₄₉	8.01 ^{+0.06} _{-0.04}
iPTF13ajg	15162 ⁺²⁵⁴ ₋₁₈₂	2.86 ^{+0.18} _{-0.09}	2820 ⁺¹³ ₋₁₀	6.18 ^{+0.02} _{-0.02}
PTF12dam	14681 ⁺³³⁰ ₋₁₄₁	1.78 ^{+0.08} _{-0.06}	2819 ⁺⁵¹ ₋₁₇	10.98 ^{+0.26} _{-0.01}

TABLE 4
 RESULTS FROM THE MCMC SIMULATION - FIXED
 λ_0

Obj.	T K	β	$\log_{10}(A)$
SN2017egm	17094 ⁺⁵⁸⁷ ₋₂₈₅	1.96 ^{+0.15} _{-0.14}	8.80 ^{+0.03} _{-0.02}
Gaia16apd	16703 ⁺⁴⁸⁰ ₋₃₉₈	0.80 ^{+0.15} _{-0.16}	8.04 ^{+0.05} _{-0.02}
iPTF13ajg	15008 ⁺²⁰⁰ ₋₇₅	2.94 ^{+0.09} _{-0.04}	6.19 ^{+0.01} _{-0.01}
PTF12dam	14681 ⁺⁸⁸ ₋₇₆	1.78 ^{+0.03} _{-0.03}	10.98 ^{+0.03} _{-0.01}

TABLE 5
THE MEASURED COLUMN DENSITIES AND ABUNDANCES

	Component 1	Component 2	Total
	at z=0.0307	at z=0.0299	
N(SII) ^a	(8.10 ± 1.90)e+14	(1.20 ± 0.18)e+15	(2.01 ± 0.26)e+15
N(FeII)	(2.13 ± 0.21)e+14	(4.80 ± 1.60)e+13	(2.61 ± 0.26)e+14
N(AlIII)	(6.31 ± 0.65)e+12	(3.64 ± 0.56)e+12	(9.95 ± 0.86)e+12
N(HI)	(3.00 ± 0.80)e+19	(3.70 ± 0.90)e+19	(6.70 ± 1.20)e+19
[S/H] _{obs} ^b	+0.30 ± 0.16	+0.38 ± 0.12	+0.34 ± 0.10
[Fe/H] _{obs}	-0.62 ± 0.12	-1.36 ± 0.18	-0.88 ± 0.09
[Al/H] _{obs}	-1.12 ± 0.12	-1.45 ± 0.13	-1.27 ± 0.09
[S/Fe] _{obs}	+0.92 ± 0.11	+1.74 ± 0.16	+1.23 ± 0.13
[S/Al] _{obs}	+1.42 ± 0.11	+1.83 ± 0.09	+1.62 ± 0.10
[S/H] _{DC} ^c	+0.59 ± 0.16	+0.98 ± 0.12	+0.74 ± 0.10
[Fe/H] _{DC}	+0.48 ± 0.12	+1.10 ± 0.18	+0.74 ± 0.09
[Al/H] _{DC}	-0.01 ± 0.12	+1.01 ± 0.13	+0.34 ± 0.09
[S/H] _{HC} ^c	+0.06 ± 0.16	+0.14 ± 0.12	+0.11 ± 0.10
[Fe/H] _{HC}	-0.86 ± 0.12	-1.60 ± 0.18	-1.12 ± 0.09
[Al/H] _{HC}	-1.35 ± 0.12	-1.68 ± 0.13	-1.50 ± 0.09
[S/H] _{corr} ^c	+0.35 ± 0.16	+0.75 ± 0.12	+0.51 ± 0.10
[Fe/H] _{corr}	+0.25 ± 0.12	+0.87 ± 0.18	+0.51 ± 0.09
[Al/H] _{corr}	-0.25 ± 0.12	+0.78 ± 0.13	+0.11 ± 0.09

^a Column density N(X) for ion X is in units of cm⁻².

^b Abundance [X/H] is in logarithmic and relative to solar abundance for ion X. It is defined as $12 + \log_{10} (N(X)/N(\text{HI})) - [X/H]_{\odot}$. Here $[S/H]_{\odot} = 7.135$, $[Fe/H]_{\odot} = 7.475$ and $[Al/H]_{\odot} = 6.44$ (Asplund et al. 2009).

^c [X/H]_{obs} is the value computed from the observed column densities without any correction. [X/H]_{DC} is for dust depletion corrected value, [X/H]_{HC} stands for the values included H ionization correction, and [X/H]_{corr} is the abundance including both dust and H ionization correction.